

Physics-Informed Neural Networks for the Point Defect Model: Solving and Inverting Passive-Film Growth Kinetics

Mohid Farooqi,¹ Ingmar Bösing,² and Conrard Giresse Tetsassi Feugmo^{3,1, a)}

¹⁾*Department of Physics and Astronomy, University of Waterloo, 200 University Avenue West, Waterloo, Ontario N2L 3G1, Canada*

²⁾*Chemical Process Engineering (CVT), University of Bremen, Bibliothekstraße 1, 28359 Bremen, Germany*

³⁾*Department of Chemistry, University of Waterloo, Waterloo, Ontario N2L 3G1, Canada*

(Dated: 26 June 2026)

Predicting how passive oxide films grow and break down is central to corrosion science and the long-term integrity of structural alloys, and the Point Defect Model (PDM) is the standard kinetic description: a stiff, coupled system of Nernst–Planck, Poisson, and Butler–Volmer equations on a moving boundary. Solving it conventionally requires specialised finite-element (FEM) solvers, and identifying its kinetic parameters requires costly experimental campaigns. Physics-informed neural networks (PINNs) are compelling here because they natively assimilate data and invert for unknown parameters, so one measurement can replace an FEM solution and yield kinetics FEM cannot. We show that PINNs solve the PDM and recover its parameters from sparse data. The problem is difficult for reasons common to stiff multiphysics systems: widely separated scales, stiff boundary conditions, and convergence to non-physical solution branches. We address these with physics-based non-dimensionalisation, which extends stable simulation from about one hour to 250 hours; NTK adaptive weighting, which compresses a four-to-six-order loss imbalance to roughly one; and a single validated anchor that selects the physical branch and brings film-thickness error below 2.2% at all five potentials. Stiff boundary-condition enforcement remains an open problem. Robustness comes from resampling the anchor each step, accuracy saturates beyond ten anchors, and the physics loss tolerates 5% measurement noise. Crucially, recoverability tracks stiffness: a boundary-stiff kinetic constant is identifiable from film-thickness data while a weakly-coupled interior coefficient is not. By turning sparse measurements into full fields and inferred kinetics, the approach reduces the experimental and computational burden of characterising passive-film growth.

Keywords: physics-informed neural networks; Point Defect Model; electrochemical passivation; Neural Tangent Kernel; stiff PDEs; multiphysics simulation

I. INTRODUCTION

Passive oxide films (spontaneously formed nanometre-thin layers on metal surfaces) are the primary electrochemical barrier separating a metal from its environment^{1–4}. Their growth kinetics determine the long-term corrosion protection of structural alloys in demanding applications including biomedical implants and nuclear reactor pressure vessels^{5–7}. Predicting how these films nucleate, thicken, and stabilise under applied potential and changing electrolyte chemistry is a central problem in corrosion science, particularly for systems where experimental access to the film/metal interface is limited.

The Point Defect Model (PDM), originally proposed by Macdonald and co-workers⁵, remains the most widely used theoretical framework for passive film growth kinetics. In the PDM, film growth and dissolution are governed by the migration and interaction of charged point defects (cation vacancies, anion vacancies, and metal interstitials) driven by electric fields and concentration gradients at both the metal/film and film/solution interfaces. Refined versions of the PDM^{8–13} replace the original assumption

of a constant electric field with an explicit solution of Poisson’s equation, making the system a fully coupled set of partial differential equations (PDEs): the Nernst–Planck equation for each defect species, Poisson’s equation for the electric potential, Butler–Volmer kinetics at both interfaces, and an ordinary differential equation (ODE) for the moving film boundary. Solving this stiff multiphysics system has required specialized finite element solvers^{10,13–16}, which are accurate but expensive for parameter sweeps and difficult to adapt to inverse problems.

Physics-informed neural networks (PINNs), introduced by Raissi, Perdikaris, and Karniadakis¹⁷, embed the governing equations directly into the training loss function, enabling mesh-free solution of PDEs without labeled training data. Two features make them well suited to the PDM in particular, and address exactly where FEM falls short: the network that solves the equations can simultaneously assimilate a data loss, and the governing constants can be made trainable, so a single PINN both fits sparse measurements and recovers unknown kinetic parameters rather than only producing a forward solution. PINNs have been applied successfully to simpler electrochemical problems: Chen and co-workers demonstrated their use for voltammetric responses^{18,19} and hydrodynamic voltammetry²⁰. PINNs have also been extended to coupled phase-field equations with moving boundaries²¹ and to phase-field

^{a)}Electronic mail: cgtetsas@uwaterloo.ca

models using NTK-based adaptive weighting²². Tutorials on PINNs for phase-field models have recently appeared in APL Machine Learning²³, and comprehensive reviews of PINN architectures and failure modes are available^{24,25}.

Despite this progress, PINNs have not yet been demonstrated on the full PDM with its combination of moving boundaries, stiff Butler–Volmer kinetics, and multi-scale variable ranges. Our systematic investigation reveals four specific failure modes that prevent purely physics-informed learning from reaching quantitative accuracy on this class of problems. The first two, scale disparity and loss imbalance, can be resolved with existing techniques. The third, stiff boundary enforcement, resists all strategies we tested. The fourth, convergence to non-physical solution branches, is resolved by adding one supervised data point. We also report two strategies that did not work (Augmented Lagrangian methods and residual network connections) and explain why, as this negative knowledge is as valuable to the community as reporting what succeeds.

The methodological contributions (non-dimensionalization, NTK-based adaptive weighting, hybrid anchoring, and loss-landscape diagnostics) are designed to transfer to any stiff coupled transport–reaction system. The PDM serves as the validation benchmark.

II. THE POINT DEFECT MODEL

A. Physical model

We follow the Refined PDM (R-PDM) of Bösing¹⁰, which resolves the electric potential explicitly and includes both cation vacancies (CV, charge $z_{CV} = -8/3$) and anion vacancies (AV, charge $z_{AV} = +2$). The fractional cation-vacancy charge arises from a mean-field treatment of mixed $\text{Fe}^{2+}/\text{Fe}^{3+}$ site occupancy in the iron oxide lattice: one vacancy compensates $\frac{2}{3}$ of an Fe^{2+} site and $\frac{1}{3}$ of an Fe^{3+} site, giving $z_{CV} = -(\frac{2}{3}\cdot 2 + \frac{1}{3}\cdot 3) = -8/3$ ¹⁰. For simplicity, electronic carriers are excluded from the PINN implementation¹⁰. The interfacial reactions for iron passivation in halide-free solution are illustrated in Fig. 1 and listed in full in the Supporting Information (SI, Section S1). The stoichiometry of chemical dissolution (R5) gives $2\text{Fe}^{3+} + \text{Fe}^{2+} + 4\text{H}_2\text{O}$, consistent with Bösing¹⁰.

B. Governing equations

The oxide film occupies the domain $[0, L(t)]$, where $L(t)$ is the film thickness at time t . Defect transport for species $i \in \{\text{CV}, \text{AV}\}$ is governed by the Nernst–Planck equation,

$$\frac{\partial C_i}{\partial t} = -\nabla \cdot \mathbf{J}_i, \quad \mathbf{J}_i = -D_i \nabla C_i - \frac{z_i F D_i C_i}{RT} \nabla \phi, \quad (1)$$

where C_i (mol m^{-3}) is the molar concentration of species i , D_i ($\text{m}^2 \text{s}^{-1}$) its diffusion coefficient, z_i its charge

number, $F = 96485 \text{ C mol}^{-1}$ the Faraday constant, $R = 8.314 \text{ J mol}^{-1} \text{ K}^{-1}$ the gas constant, T the absolute temperature, and ϕ (V) the electric potential. The potential satisfies Poisson’s equation,

$$-\nabla \cdot (\epsilon \nabla \phi) = F \sum_i z_i C_i, \quad (2)$$

where ϵ (F m^{-1}) is the dielectric permittivity of the oxide. Interfacial reaction rates k_j follow Butler–Volmer kinetics,

$$k_j = k_j^0 \exp\left(-\alpha_j \frac{F}{RT} \eta_j\right), \quad (3)$$

where k_j^0 is the pre-exponential rate constant, α_j the charge transfer coefficient, and $\eta_j = E - E_j^0$ the overpotential for reaction j , with E the applied potential (V) and E_j^0 the equilibrium potential (V). The single-exponential form retains only the dominant direction for each interfacial reaction: under the anodic conditions of passive film growth, metal oxidation at the metal/film interface and dissolution at the film/solution interface are both strongly irreversible ($|\eta_j| \gg RT/F$), so the back-reaction term is negligible¹⁰. Film growth couples to the defect fluxes via

$$\frac{dL}{dt} = \Omega \sum_j \nu_j k_j, \quad (4)$$

where Ω ($\text{m}^3 \text{ mol}^{-1}$) is the molar volume of the oxide and ν_j the stoichiometric volume contribution of reaction j . All boundary and initial conditions, together with all parameter values, are given in the SI (Section S3).

Figure 1(a) illustrates the defect reactions at the metal/film (m/f) and film/solution (f/s) interfaces. Species notation: Fe, iron atom in the metal; Fe_{ox} , iron atom in the oxide lattice; $V_{\text{Fe}}^{8/3-}$, iron cation vacancy; V_{O}^{2-} , doubly-charged oxygen vacancy; e^- and h^+ , electron and hole carriers; Fe^{n+} , iron ion in solution. The flux boundary conditions at the f/s interface are $J_{CV}(x=L) = -k_3$ and $J_{AV}(x=L) = k_4 c_{AV}$. Panel (b) shows the potential distribution across the Fe/passive film/solution interface, with drops $\varphi_{m/f}$ and $\varphi_{f/s}$ localised at the two boundaries.

III. PINN METHODOLOGY

A. Non-dimensionalization

Scale disparity is the first obstacle for PINNs applied to the PDM: spatial coordinates are on the order of one nanometre (10^{-9} m), concentrations span many orders of magnitude, and simulation times can reach 10^5 s . In 32-bit floating-point arithmetic, gradients at nanometre length scales fall below machine precision, causing the network to learn flat profiles instead of the correct spatial variation (Fig. 9).

We remove these disparities by rescaling all variables with characteristic scales grounded in the physics of the

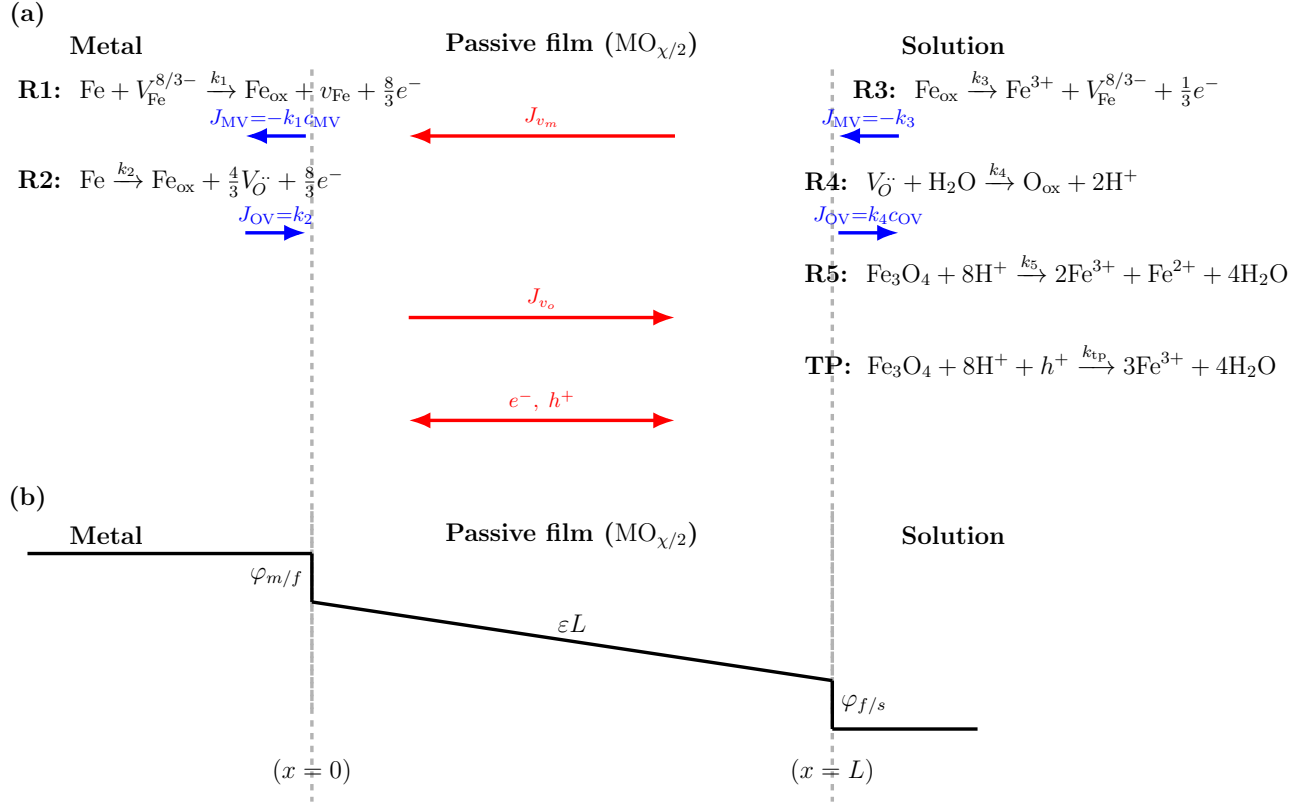


FIG. 1: (a) PDM defect reactions at the metal/film and film/solution interfaces for iron passivation in halide-free solution. (b) Schematic potential distribution across the Fe/passive film/solution interface. Species notation and boundary conditions are defined in the text.

system:

$$L_c = 10^{-9} \text{ m} \quad (\text{one nanometre, initial film thickness}), \quad (5)$$

$$t_c = \frac{L_c^2}{D_{CV}} \quad (\text{diffusive time scale}), \quad (6)$$

$$c_c = 10^{-5} \text{ mol m}^{-3} \quad (\text{reference concentration}), \quad (7)$$

$$\phi_c = \frac{RT}{F} \approx 0.0257 \text{ V at 298 K} \quad (\text{thermal voltage}). \quad (8)$$

The choice $\phi_c = RT/F$ is natural for electrochemical systems because it makes the Butler–Volmer exponents dimensionless with coefficients equal to the charge transfer coefficient times the charge number, both of order one. The dimensionless variables are

$$\hat{x} = \frac{x}{L_c}, \quad \hat{t} = \frac{t}{t_c}, \quad \hat{c}_i = \frac{C_i}{c_c}, \quad \hat{\phi} = \frac{\phi}{\phi_c}, \quad \hat{L} = \frac{L}{L_c}. \quad (9)$$

With this scaling, all variables remain within $\mathcal{O}(1)$ to $\mathcal{O}(100)$ throughout the domain, which is the range where floating-point arithmetic is reliable. The practical benefit is dramatic: dimensional models become numerically unstable at around 3600 s, whereas the non-dimensional

model runs stably to 900 000 s, a factor of 250 improvement in temporal range. The non-dimensional governing equations, boundary conditions, and the derived dimensionless parameters (Péclet numbers, Damköhler number, and screening ratio) are given in full in the SI (Section S2).

B. Segregated network architecture

Assigning a single network to represent all fields concentrates conflicting gradient signals in one set of weights. Following the approach used for coupled phase-field²¹ and microfluidic systems²⁶, we use a *segregated* architecture in which each physical field has its own dedicated network. Specifically, $\mathcal{U}_\phi(\hat{x}, \hat{t}, E)$ predicts the electric potential, $\mathcal{U}_{CV}(\hat{x}, \hat{t}, E)$ the cation vacancy concentration, $\mathcal{U}_{AV}(\hat{x}, \hat{t}, E)$ the anion vacancy concentration, and $\mathcal{U}_L(\hat{t}, E)$ the film thickness. The spatial input \hat{x} is omitted from \mathcal{U}_L because film thickness depends only on time and the applied potential, not on position within the film. Each network uses five hidden layers of 20 neurons with Swish activation functions²⁷, chosen for its smooth gradient properties relative to tanh. The four field networks together hold approximately 9k trainable parameters; this

5×20 depth and width follows the configuration recommended by Chen et al.²² for NTK-weighted PINNs on coupled-field problems, and preliminary tests over the range 4×20 to 6×32 produced no statistically significant change in the converged hybrid error. The applied potential E is sampled once per mini-batch and shared across all collocation points in that batch, correctly encoding the experimental reality that E is spatially uniform. This also means the trained model can sweep the entire polarisation curve in a single inference pass without retraining. The PINNACLE training loop is shown in Fig. 2. At each step, collocation points (\hat{x}, \hat{t}, E) are sampled and passed to the four segregated networks. Their outputs are used to evaluate the PDE, BC, IC, and film-growth residuals. Every 100 steps, NTK adaptive weights are recomputed and the loss components are rebalanced before the Adam parameter update is applied. In hybrid mode, a single FEM-validated film-thickness point is included as an anchor loss term $\mathcal{L}_{\text{data}}$, weighted identically to the film-growth loss.

C. Loss function

The training loss combines PDE residuals (interior), boundary conditions (BC), initial conditions (IC), and a film-growth ODE term. For each state variable $j \in \{\text{CV}, \text{AV}, \phi\}$, the interior loss penalises the discrepancy between the predicted time derivative and the PDE operator \mathcal{N}_j :

$$\mathcal{L}_{\text{int}} = \sum_j \frac{1}{N_{\text{int}}} \sum_{i=1}^{N_{\text{int}}} \left| \mathcal{N}_j(\mathcal{U}_j(x_i, t_i)) - \frac{\partial \mathcal{U}_j(x_i, t_i)}{\partial t} \right|^2, \quad (10)$$

$$\mathcal{L}_{\text{BC}} = \sum_j \frac{1}{N_{\text{BC}}} \sum_{i=1}^{N_{\text{BC}}} |\partial \Omega_j(\mathcal{U}_j(x_i, t_i))|^2, \quad (11)$$

$$\mathcal{L}_{\text{IC}} = \sum_j \frac{1}{N_{\text{IC}}} \sum_{i=1}^{N_{\text{IC}}} |\mathcal{I}_j(\mathcal{U}_j(x_i))|^2, \quad (12)$$

$$\mathcal{L}_{\text{film}} = \frac{1}{N_{\text{film}}} \sum_{i=1}^{N_{\text{film}}} \left| \frac{\partial \mathcal{U}_L(t_i)}{\partial t} - \frac{dL}{dt}(t_i) \right|^2, \quad (13)$$

$$\mathcal{L}_{\text{total}} = w_{\text{int}} \mathcal{L}_{\text{int}} + w_{\text{BC}} \mathcal{L}_{\text{BC}} + w_{\text{IC}} \mathcal{L}_{\text{IC}} + w_{\text{film}} \mathcal{L}_{\text{film}}. \quad (14)$$

The scalar weights w_k are updated adaptively using the NTK framework described in Sec. III D.

D. NTK-based adaptive loss balancing

Even after non-dimensionalization, the Poisson loss dominates the transport losses by four to six orders of magnitude under uniform weighting (Fig. 10(a,b)). When this happens, the optimizer effectively ignores the minority-

loss terms and the PINN learns only the dominant equation.

The Neural Tangent Kernel (NTK) framework provides a principled way to balance this. Introduced by Jacot, Gabriel, and Hongler²⁸, the NTK describes how a neural network's outputs change with respect to small parameter perturbations during training. In the infinite-width limit, training is equivalent to kernel gradient descent with a fixed kernel. For finite networks, the NTK provides a useful approximation: the eigenvalues of the NTK matrix for each loss term determine the effective learning rate of that term. If one term's NTK eigenvalues are much larger than another's, the optimizer updates that term aggressively and neglects the other, the mechanism by which Wang et al.²⁹ explain why PINNs often fail to train. Equalising the NTK traces across loss components therefore equalizes the effective learning rates.

Concretely, let $\theta \in \mathbb{R}^M$ denote the network parameter vector. For loss component k evaluated at N_k collocation points $\{(x_n, t_n, E_n)\}_{n=1}^{N_k}$, define the per-point residual Jacobian matrix

$$\mathbf{J}_k \in \mathbb{R}^{N_k \times M}, \quad (\mathbf{J}_k)_{nm} = \frac{\partial r_k(x_n, t_n, E_n)}{\partial \theta_m}, \quad (15)$$

where $r_k(x_n, t_n, E_n)$ is the per-point residual. The NTK matrix is the outer product

$$\mathbf{K}_k = \mathbf{J}_k \mathbf{J}_k^\top \in \mathbb{R}^{N_k \times N_k}, \quad (16)$$

and its trace,

$$\text{tr}(\mathbf{K}_k) = \sum_{n=1}^{N_k} \sum_{m=1}^M \left(\frac{\partial r_k(x_n, t_n, E_n)}{\partial \theta_m} \right)^2, \quad (17)$$

measures the total sensitivity of component k to parameter changes. We set

$$w_k(s) = \frac{N_k^{-1} \text{tr}(\mathbf{K}_k(s))}{\sum_j N_j^{-1} \text{tr}(\mathbf{K}_j(s))}, \quad (18)$$

following the formulation of Chen et al.²². Computing the full Jacobian at every step is prohibitive ($\mathcal{O}(N_k \times M)$ memory per component), so we use a mini-batch approximation: by the central limit theorem³⁰, the diagonal mean of \mathbf{K}_k over a random sub-batch of size b_k converges to the true mean as $b_k \rightarrow N_k$. We select b_k such that the coefficient of variation of the estimate is below 0.2²², and recompute weights every 100 training steps for computational efficiency.

The realised sub-batch sizes are $b_{\text{int}} = 1024$, $b_{\text{BC}} = 512$, $b_{\text{IC}} = 512$, and $b_{\text{film}} = 1024$. Recomputing the NTK weights every 100 steps raises the mean per-step training cost from 34.8 ms under uniform weighting to 48.5 ms, and the peak GPU memory from 237 to 805 MB: an overhead of roughly 14 ms/step and 570 MB that buys the loss balancing above. Two numerical-stability measures are also applied. First, per-component spike

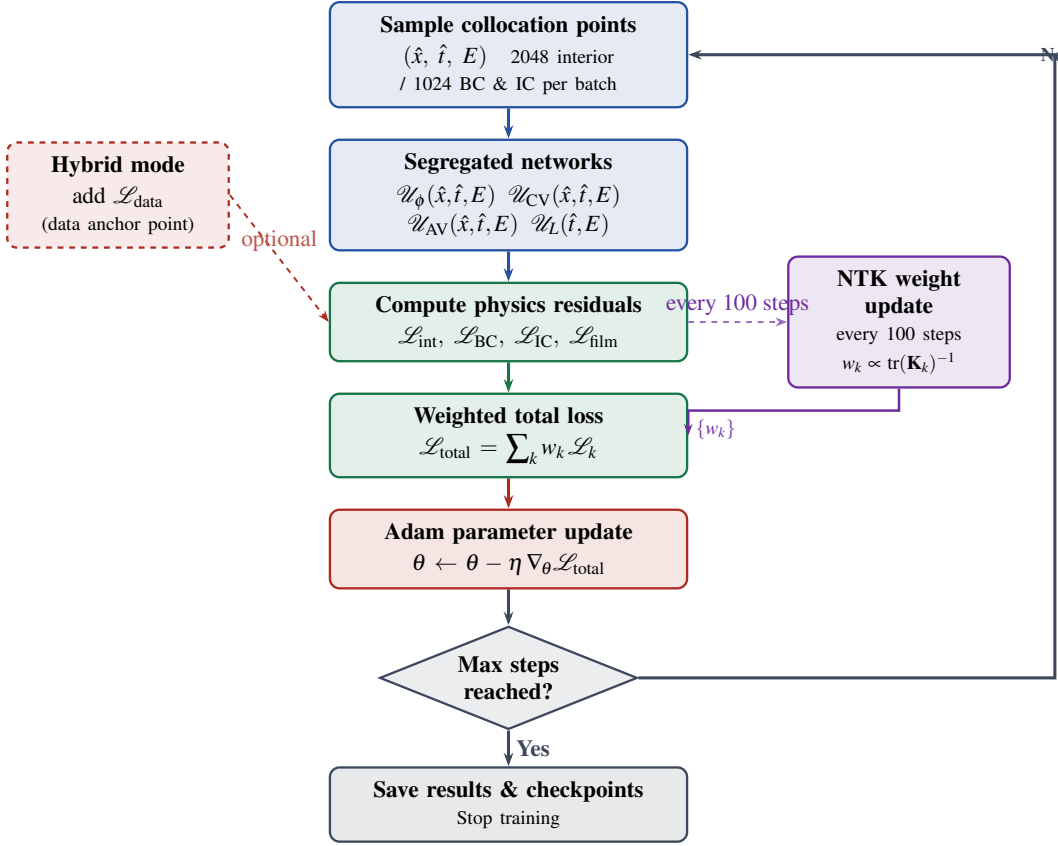


FIG. 2: PINNACLE training loop with four segregated networks and NTK adaptive loss weighting. The dashed red path indicates hybrid mode, in which a single FEM anchor point is added to the loss.

rejection: any step whose film-physics, boundary, interior, or initial loss component exceeds 10^{15} is skipped, with its gradients zeroed and the Adam state left unchanged, which protects the optimiser from non-physical transients early in training without altering the kinetics. Second, the FEM data-matching term $\mathcal{L}_{\text{data}}$ is added to the weighted physics sum without rescaling, so the anchor constraint is always enforced.

E. Hybrid training with minimal data

As discussed in Sec. VD, pure PINN training, despite converging successfully, settles onto the wrong solution branch of the PDM equations. To resolve this, we add a single supervised data term

$$\mathcal{L}_{\text{data}} = |\mathcal{U}_L(t^*, E^*) - L^*|^2 \quad (19)$$

to the total loss, where (t^*, E^*, L^*) is one FEM-validated point. This term carries the same adaptive NTK weight as the film loss. The sensitivity to this anchor is quantified in Sec. IV D: the result is reproducible when the anchor is resampled at each step, whereas a single fixed anchor is placement-sensitive. The PINN already encodes the

correct physics and needs only the anchor to select the physical solution branch. Combining a sparse set of supervised observations with a physics loss is a well-studied strategy for inverse and data-scarce PDE problems: Raissi et al.³¹ demonstrated it for hidden fluid mechanics, Chen, Liu, and Sun³² recovered governing equations from as few as $\mathcal{O}(10^2)$ observations, and recent work has quantified the data requirements for surrogate modelling of stirred tanks³³ and 3D flow-thermal problems³⁴; Cuomo et al.³⁵ give a broad survey.

The complete training procedure is summarised in Algorithm 1.

Algorithm 1 PINNACLE: PINN training with NTK adaptive loss balancing

```

1: Input: networks  $\{\mathcal{U}_\phi, \mathcal{U}_{CV}, \mathcal{U}_{AV}, \mathcal{U}_L\}$ , parameter vector  $\theta$ 
2: Initialise: Adam optimizer,  $w_k \leftarrow 1$  for all  $k$ , step  $s \leftarrow 0$ 
3: while  $s < s_{\max}$  do
4:   Sample collocation points:  $\mathcal{X}_{\text{int}}$  (2048),  $\mathcal{X}_{\text{BC}}$  (1024),
 $\mathcal{X}_{\text{IC}}$  (1024),  $\mathcal{X}_{\text{film}}$  (2048)
5:   for each point set  $\mathcal{X}_k$  do
6:     Compute predictions and PDE/BC/IC residuals  $r_k$ 
7:      $\mathcal{L}_k \leftarrow \frac{1}{|\mathcal{X}_k|} \sum_i |r_k^{(i)}|^2$ 
8:   end for
9:   if  $s \bmod 100 = 0$  then
10:    for each component  $k$  do
11:      Draw random sub-batch of size  $b_k$  from  $\mathcal{X}_k$ 
12:      Compute Jacobian  $\mathbf{J}_k$  (per-point gradients w.r.t.
 $\theta$ ) on sub-batch
13:       $\lambda_k \leftarrow \frac{1}{b_k} \text{tr}(\mathbf{J}_k \mathbf{J}_k^\top)$ 
14:    end for
15:     $w_k \leftarrow \lambda_k / \sum_j \lambda_j$  ▷ renormalize weights
16:  end if
17:   $\mathcal{L}_{\text{total}} \leftarrow \sum_k w_k \mathcal{L}_k$ 
18:   $\theta \leftarrow \theta - \eta \nabla_{\theta} \mathcal{L}_{\text{total}}$  ▷ Adam step
19:   $s \leftarrow s + 1$ 
20: end while
21: Return: trained networks  $\{\mathcal{U}_\phi^*, \mathcal{U}_{CV}^*, \mathcal{U}_{AV}^*, \mathcal{U}_L^*\}$ 

```

IV. RESULTS

A. Benchmark setup

We validate against FEM solutions of the R-PDM computed by Bösing¹⁰ in COMSOL Multiphysics with adaptive meshing to handle the moving boundary. The FEM boundary conditions and their convergence are documented in that reference. We evaluate film thickness predictions across applied potentials $E \in [0.1, 1.8]$ V and simulation times up to 9×10^5 s (≈ 250 hours). All PINN models are trained for 50 000 Adam steps at a learning rate of 10^{-3} . For convergence verification, we additionally ran training at 100 000 steps and confirmed that the hybrid error changes by less than 0.1 percentage point; the results reported here are converged.

B. Pure PINN results

Figure 3 shows the field profiles predicted by the pure NTK-weighted PINN. The model reproduces the correct qualitative behavior: film growth is exponential and voltage-dependent, and the potential and concentration profiles evolve consistently with the physical picture. At $E = 0.1$ V, growth is minimal; at higher potentials the film grows faster, as expected from the Butler–Volmer kinetics.

However, a direct comparison with the FEM reference reveals a large quantitative discrepancy (Fig. 4). The PINN overestimates film thickness by one to two orders of

magnitude at all voltages tested (Table I). At $E = 0.1$ V it predicts 32 nm against the FEM reference of 1.27 nm; at $E = 1.8$ V it predicts 821 nm against 16.1 nm. This is not a training failure: losses converge cleanly and the predicted potential profiles are dimensionally plausible¹⁰. Instead, we interpret this as convergence to a different branch of the solution manifold, as discussed in Sec. VC.

C. Hybrid PINN results

Adding a single FEM data point ($t^* = 150\,000$ s, $E^* = 0.1$ V, $L^* = 1.27$ nm), chosen at random without optimisation, transforms the results dramatically. The hybrid predictions match the FEM reference closely at every voltage tested (Fig. 5). At $E = 0.1$ V the error drops from 2412% to 0.32% and $R^2 = 0.90$; comparable improvements hold across the full voltage range (Table I).

The R^2 values are computed over the full transient time series, not just the final film thickness. Lower values at intermediate voltages (e.g., $R^2 = 0.87$ at 0.4 V) reflect the fact that the FEM transient at those conditions is short: the initial mismatch during the first few thousand seconds carries proportionally more weight in the R^2 metric, while the final film thickness error at the same voltage is below 1%.

TABLE I: Film-thickness error (final value) and R^2 over the full transient for the pure PINN and the hybrid PINN at five applied potentials. The improvement factor is the ratio of pure to hybrid error.

E (V)	Pure (%)	Hybrid (%)	Improvement	R^2
0.1	2412	0.32	7537 \times	0.8975
0.4	4707	0.97	4852 \times	0.8708
1.0	5708	0.80	7135 \times	0.9123
1.6	5218	2.18	2393 \times	0.9428
1.8	5001	0.38	13160 \times	0.9891

D. Robustness to anchor placement

The hybrid result is robust in two senses that we quantify separately. First, it is reproducible across independent random-anchor streams: we repeated the hybrid training for seven independent random seeds, each resampling one FEM anchor point per step from the full solution. Six of the seven converge to the physical branch, with whole-curve relative film-thickness errors (averaged over the five test voltages) between 1.7% and 14.6% (mean 4.3%, with five of the six clustering tightly at $2.3 \pm 0.5\%$; Fig. 5); the remaining seed converges to a non-physical branch (240%), an initialisation-driven failure rather than a property of the anchor. An independent re-run of four of these seeds under a fixed 50,000-step protocol reproduces the same statistics (three of four converge, $4.3 \pm 3.1\%$).

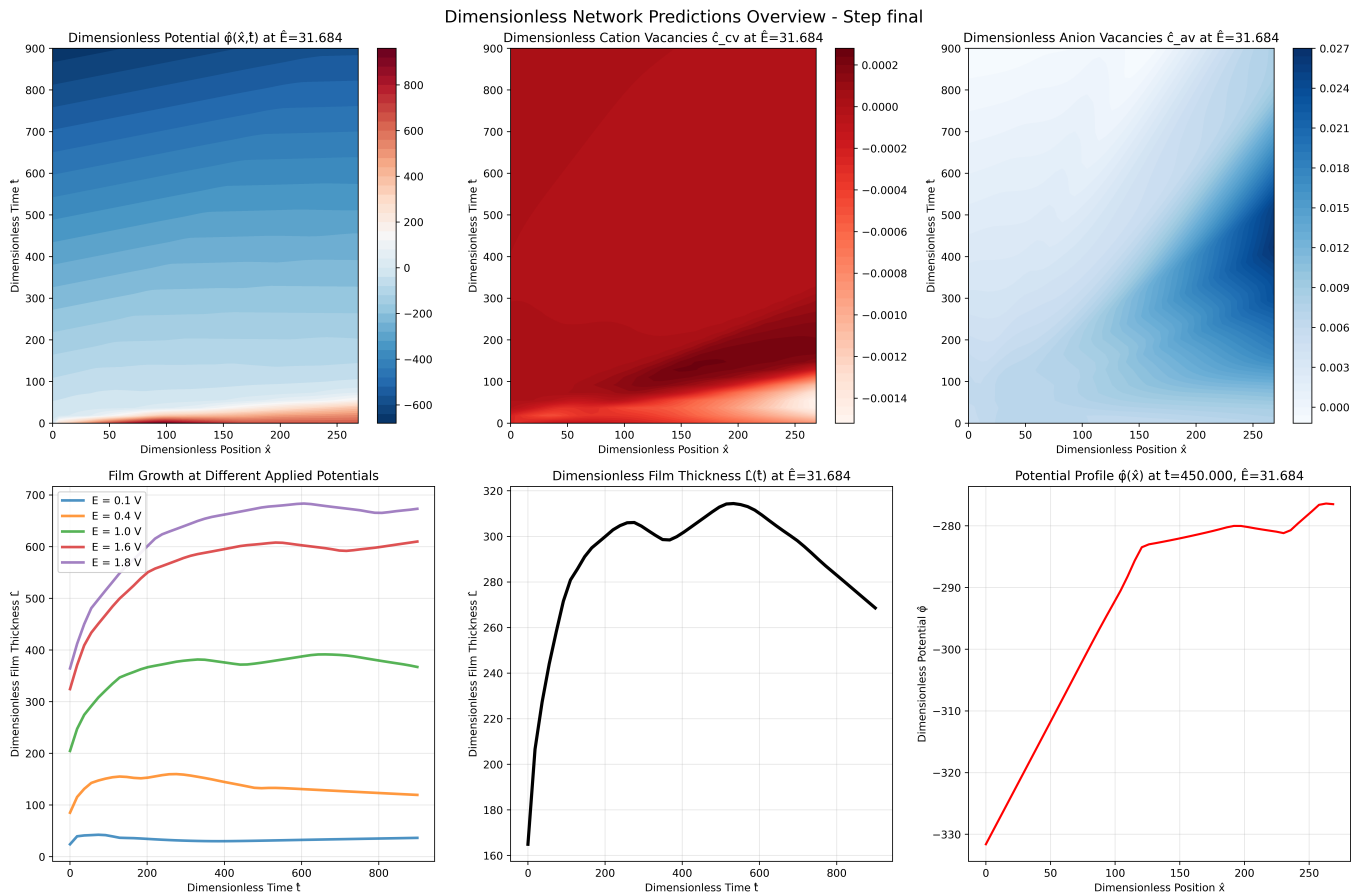


FIG. 3: Pure PINN predictions (NTK weighting, 250 hours). Top row: dimensionless potential, cation vacancy, and anion vacancy profiles at selected times. Bottom row: film thickness versus time at representative potentials. Qualitative trends are physically plausible; absolute scale does not match the FEM (see Fig. 4).

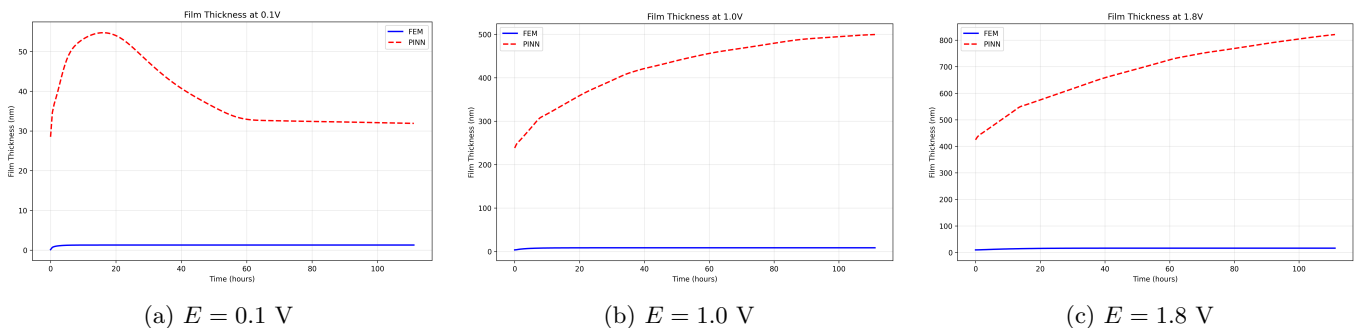


FIG. 4: Pure PINN vs. FEM film thickness at three applied potentials. The PINN captures the correct exponential shape and voltage ordering, but overestimates the absolute scale by factors of 20–50.

Second, this robustness stems specifically from *resampling* the anchor at every step, not from any single point being sufficient. When one FEM point is instead held fixed for the entire run, the error is large and strongly dependent on where that point is placed: a sweep over five fixed positions in the (t, E) domain gives errors from 84% to 353% (Table II). The redraw-every-step scheme therefore behaves less like a single supervised label and more like a

stochastic regulariser that repeatedly nudges the solution toward the physical branch.

E. Data efficiency

We next varied the number of fixed FEM anchor points N_{data} supplied during training, from $N_{\text{data}} = 0$ (pure

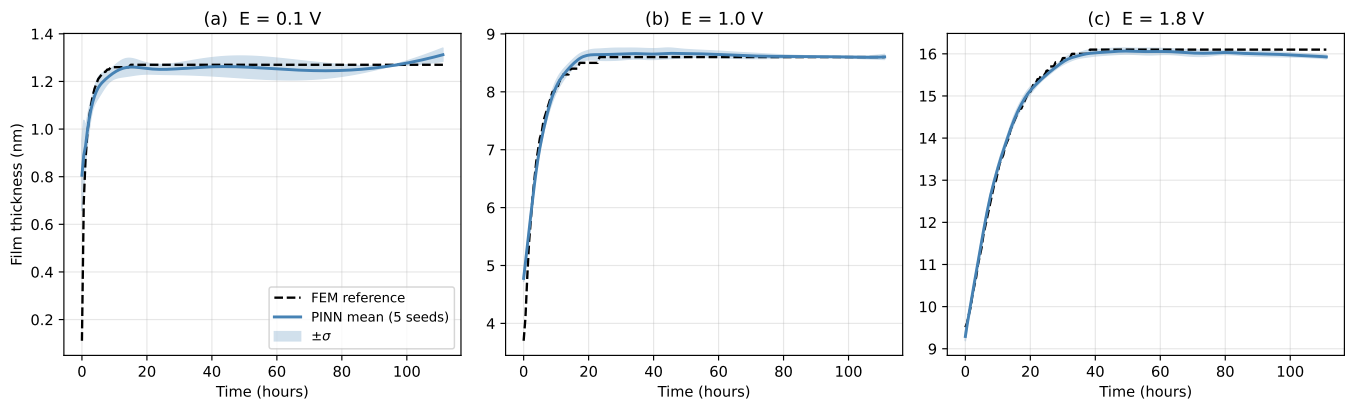


FIG. 5: Hybrid PINN vs. FEM: a single anchor steers the PINN onto the physical solution branch at all voltages, and the result is reproducible. Mean PINN film-thickness prediction (solid) with $\pm\sigma$ band (shaded) over the five converged random-anchor seeds, against the FEM reference (dashed), at (a) 0.1 V, (b) 1.0 V, and (c) 1.8 V. The mean tracks FEM across the full transient, with the spread widest at the hardest low-voltage case.

TABLE II: Single fixed-anchor position sweep. A lone FEM anchor is held fixed throughout training at the indicated (t^* , E^*); the error is the whole-curve relative L_2 film-thickness error averaged over the five test voltages. Contrast with the $\sim 2\text{--}4\%$ obtained when the anchor is resampled every step.

Anchor	t^* (ks)	E^* (V)	Error (%)
early, low E	2	0.1	353
mid, low E	200	0.1	84
late, low E	380	0.1	85
mid, mid E	200	1.0	104
mid, high E	200	1.6	341

PINN) up to 50, averaging over three random seeds at each level (Fig. 6). With no anchor the error is enormous and highly variable (mean 518%), confirming the branch ambiguity. A single fixed anchor already reduces the error to about 66%, and the error then falls steadily: 36% at $N_{\text{data}} = 3$, 18% at $N_{\text{data}} = 10$, and 6.5% at $N_{\text{data}} = 50$. Returns diminish beyond roughly ten anchor points, so a handful of FEM evaluations already captures most of the available accuracy.

F. Noise robustness

Experimental film-thickness data carry measurement uncertainty, so we tested how multiplicative Gaussian noise on the anchor value, $L^* \rightarrow L^*(1 + \varepsilon)$ with $\varepsilon \sim \mathcal{N}(0, \sigma^2)$, propagates into the solution (Fig. 7, $N_{\text{data}} = 10$, three seeds per level). The physics loss acts as a denoiser: the error rises only gradually, from 17.9% at $\sigma = 0$ to 23.9% at $\sigma = 5\%$, and remains usable ($\sim 30\text{--}46\%$) even at $\sigma = 50\%$. The film-growth physics constrains the solution enough that a noisy anchor still selects the correct branch.

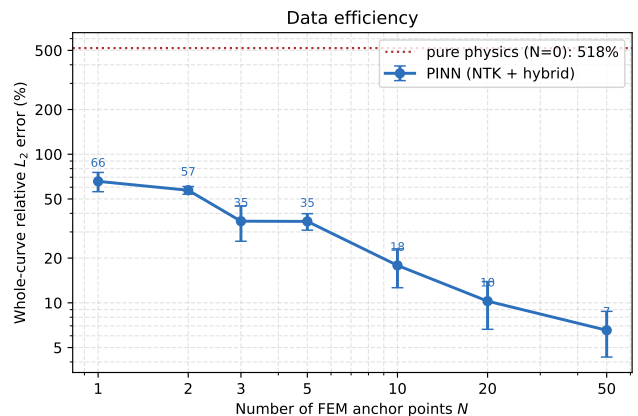


FIG. 6: Data efficiency. Whole-curve relative L_2 film-thickness error (mean \pm s.d. over three seeds, averaged over the five test voltages) versus the number of fixed FEM anchor points N_{data} , on log-log axes. Returns diminish beyond $N_{\text{data}} \approx 10$.

G. Inverse problem: parameter recovery

The same framework supports inverse problems. Rather than taking the kinetic parameters as known, we treat a chosen parameter as an unknown, represent it as a learnable variable in \log_{10} space, and optimise it by gradient descent alongside the network weights against a small set of $L(t)$ observations. To keep the coupled solve stable we use a two-stage schedule: the networks are trained first with the parameter held at its initial guess, after which the networks are frozen and only the parameter is updated. We recover one parameter at a time, since the joint recovery of several kinetic constants from a single observable is ill-posed.

The outcome is governed by which loss term the pa-

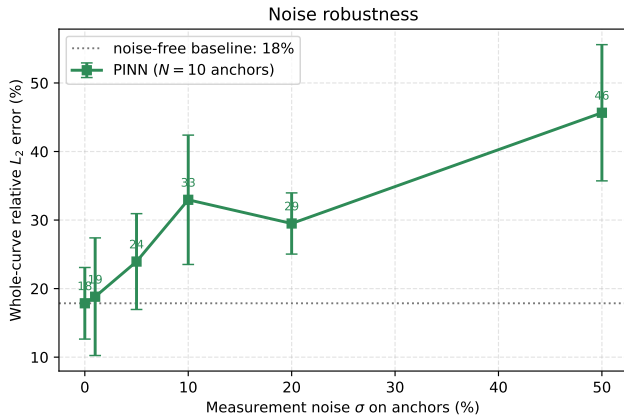


FIG. 7: Noise robustness. Whole-curve relative L_2 film-thickness error (mean \pm s.d. over three seeds, averaged over the five test voltages) versus the standard deviation σ of multiplicative Gaussian noise on the anchor measurement, at $N_{\text{data}} = 10$.

parameter is stiff in. The rate constant k_2^0 is *boundary-stiff*: it enters the film-growth law, Eq. (4), directly through the exponential Butler–Volmer term, so it controls the observable $L(t)$ strongly. Starting from an initial guess ten times the true value (3.6×10^{-5} against a true 3.6×10^{-6}), the optimiser drives k_2^0 monotonically down through more than a decade of error (Fig. 8) and settles within about a third of the true value: 2.3×10^{-6} (37% error) from observations at a single voltage, and 4.8×10^{-6} (34% error) when three voltages are observed. The residual error is set by the forward model’s own $L(t)$ fit rather than by the number of observation voltages, and in both cases k_2^0 is recovered to the correct order of magnitude.

The diffusion coefficient D_{CV} behaves oppositely. It is *interior-stiff*: it appears in the Nernst–Planck transport equation, Eq. (1), and influences $L(t)$ only indirectly, through the vacancy flux that feeds the moving boundary. Starting from a guess five times the true value (5×10^{-21} against a true 1×10^{-21}), the parameter barely moves and in fact drifts further from the true value (5.8×10^{-21} , a 483% error): the film-thickness observations simply do not constrain it. Recovering D_{CV} would require observations of the interior concentration field, not of $L(t)$ alone.

These two cases show that parameter recoverability in this system tracks stiffness: a parameter that drives the observable directly is identifiable from sparse film-thickness data, whereas one that couples to the observable only weakly is not. This provides a practical diagnostic for any inverse PINN problem, indicating which parameters a given measurement can constrain before any optimisation is attempted.

V. FAILURE MODES AND SOLUTIONS

A. Scale disparity and non-dimensionalization

Without non-dimensionalization, spatial coordinates ($\sim 10^{-9}$ m) and concentration differences fall below the resolution of 32-bit floating-point arithmetic. The network then learns constant or nearly constant potential profiles (Fig. 9), in clear violation of the physical boundary conditions. Furthermore, dimensional models become numerically unstable beyond about 3600 s, whereas the non-dimensional model remains stable to 9×10^5 s, a factor-of-250 improvement in temporal reach.

Non-dimensionalization with physics-based characteristic scales (Eqs. (5)–(8)) resolves both problems. Malekjani et al.³⁶ confirm, for a similar multi-scale problem, that physics-based rescaling consistently outperforms statistical normalization.

B. Loss imbalance and NTK weighting

Under uniform weighting, the Poisson loss dominates the transport losses by four to six orders of magnitude (Fig. 10(a,b)). The NTK-weighted training brings the Poisson and transport losses to within one order of magnitude of each other, and all components show monotonically decreasing trends (Fig. 10(c–e)). Boundary-condition losses remain noisier because the moving boundary continuously generates new, previously unseen sampling coordinates at each step. Despite this residual oscillation in the BC loss, the converged solution is physically plausible. Complete loss curves for all three weighting configurations are reproduced in the SI (Section S5) for reference.

C. Stiff boundary conditions: an open problem

Some boundary conditions resist convergence regardless of the weighting strategy applied. The NTK approach reduces their assigned weight, which paradoxically means the optimizer effectively ignores the hardest constraints. This is the mechanism that leads to qualitatively correct but quantitatively wrong solutions in pure PINN mode.

We tested the Augmented Lagrangian (AL) method³⁷, which reformulates PINN training as a constrained optimisation problem,

$$\max_{\boldsymbol{\lambda}} \min_{\boldsymbol{\theta} \in \mathbb{R}^M} [\mathcal{L}_{\text{PDE}}(\boldsymbol{\theta}) + \beta \|\mathbf{c}(\boldsymbol{\theta})\|_2^2 + \langle \boldsymbol{\lambda}, \mathbf{c}(\boldsymbol{\theta}) \rangle], \quad (20)$$

where $\mathbf{c}(\boldsymbol{\theta}) \in \mathbb{R}^{N_c}$ is the vector of constraint residuals (boundary and initial conditions), $\beta > 0$ a fixed penalty parameter, $\boldsymbol{\lambda} \in \mathbb{R}^{N_c}$ the vector of Lagrange multipliers, and $\langle \cdot, \cdot \rangle$ the Euclidean inner product. The Lagrange multipliers adapt to enforce the constraints, while the PDE residual is minimised in the interior. Theory guarantees convergence for the Helmholtz, viscous Burgers,

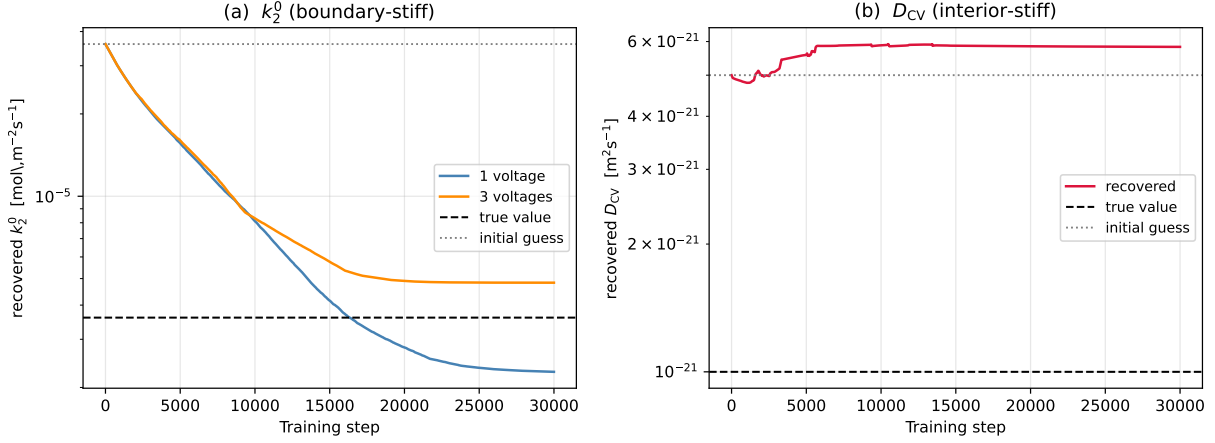


FIG. 8: Parameter recovery during training. (a) The boundary-stiff rate constant k_2^0 descends monotonically from a ten-fold initial overestimate toward its true value (dashed) under observations at one and at three voltages, settling within about a third of the true value. (b) The interior-stiff diffusion coefficient D_{CV} barely moves and drifts away from its true value (dashed, an order of magnitude below the initial guess), confirming that film-thickness data alone do not constrain it.

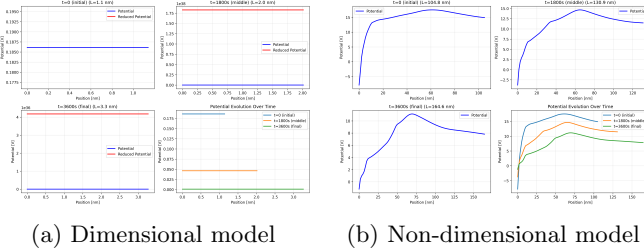


FIG. 9: Potential profiles at representative times. The dimensional model learns flat (constant) profiles due to floating-point underflow at nanometre scales. The non-dimensional model captures the correct spatial gradient.

and Klein–Gordon equations³⁷, but neither Adam nor L-BFGS converged on the PDM with this formulation.

We also tested staged training in which NTK weighting is used for a warm-up phase followed by AL³⁸, but this also failed to converge. The likely reason is a saddle-point instability: the AL penalty pushes constraints toward zero independently of whether the interior loss is satisfied, creating dynamics that gradient descent cannot escape from in this strongly coupled system. Robust constraint enforcement for stiff multiphysics PINNs is left as an open problem.

To pinpoint which constraint is responsible, we logged the six per-interface weighted boundary residuals (the cation-vacancy, anion-vacancy, and potential constraints at each of the metal/film and film/solution interfaces) throughout training (Fig. 11). The cation-vacancy and potential residuals settle below 10^{-4} at both interfaces, whereas the anion-vacancy residual undergoes a regime change near step 1.3×10^4 and locks at $\mathcal{O}(10^5)$, four to

five orders of magnitude above every other component. This isolates the anion-vacancy boundary condition as the single unenforced constraint, consistent with the loss-landscape diagnostic below, and as the proximate cause of the initialisation-driven divergences seen in Sec. IV D.

D. Pathological solution convergence: the hybrid remedy

Pure PINN training converges cleanly, but to the wrong solution. The systematic overprediction across all voltages, combined with the qualitatively correct exponential growth and voltage dependence, is consistent with several non-exclusive explanations, and we present non-uniqueness as a hypothesis rather than a settled conclusion. The most direct reading is non-uniqueness of the PDM’s solution manifold: the coupled Nernst–Planck and Poisson equations under exponential Butler–Volmer boundary conditions need not admit a unique solution, so the optimiser may settle on a branch that satisfies the physics to within tolerance but at the wrong absolute scale. The same observations are, however, equally consistent with (i) incomplete enforcement of the stiff anion-vacancy boundary condition, which the boundary-residual diagnostic (Fig. 11) identifies as the dominant unsatisfied constraint; (ii) spectral bias of the Adam-trained network toward low-frequency modes early in training; or (iii) optimisation bias on the residual-loss manifold. Distinguishing these rigorously would require an analytical study of the PDM solution structure, which is beyond the present scope; either way, the single anchor resolves the symptom by selecting the physical branch.

FEM avoids this by implicitly restricting the solution space through spatial discretization and physically motivated initialization. A PINN starting from random

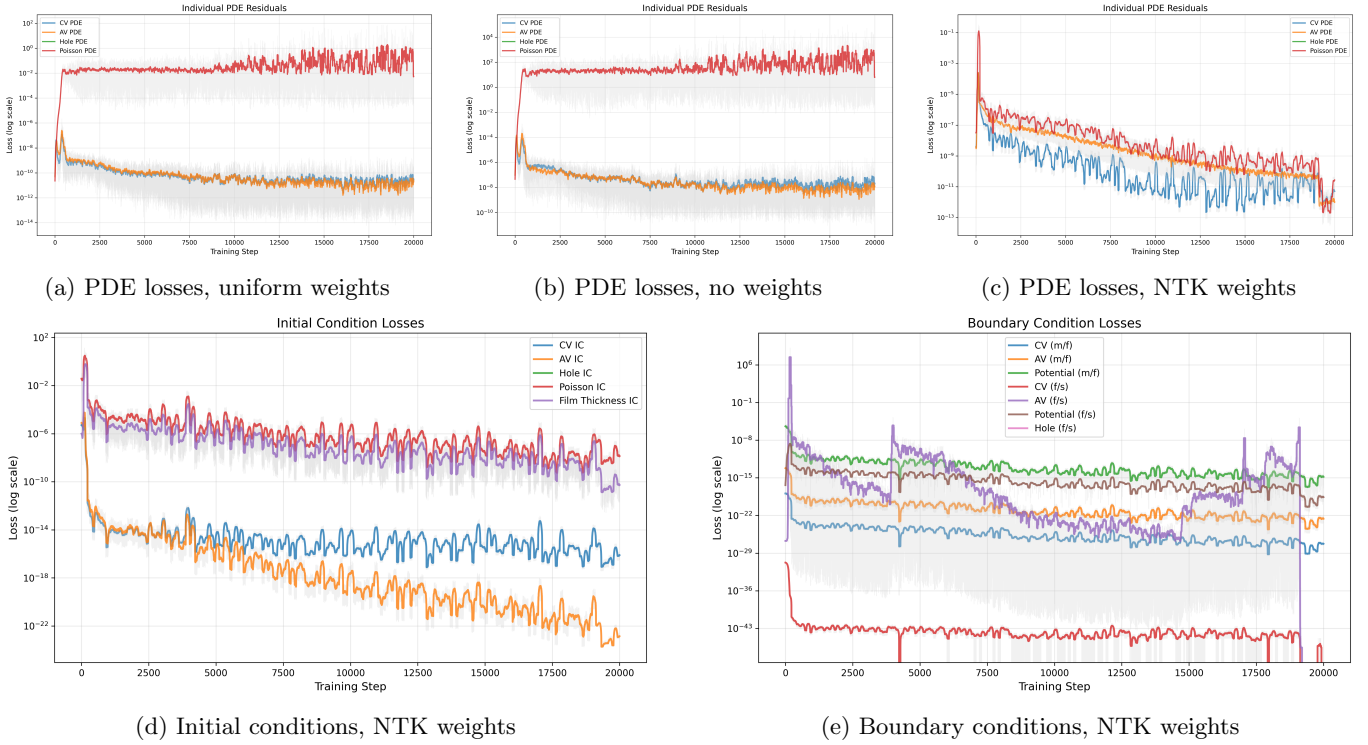


FIG. 10: Training loss evolution. Top row: under uniform weighting (a) and no weighting (b), the Poisson PDE residual (red) dominates by four to six orders of magnitude, starving the transport equations of gradient information; NTK weighting (c) brings all PDE components to within one order of magnitude of each other. Bottom row: NTK weighting also produces well-behaved initial conditions (d) and boundary conditions (e), though the BC loss remains noisier due to the continuously expanding moving-boundary domain. Solid lines are moving averages; translucent fills show raw values.

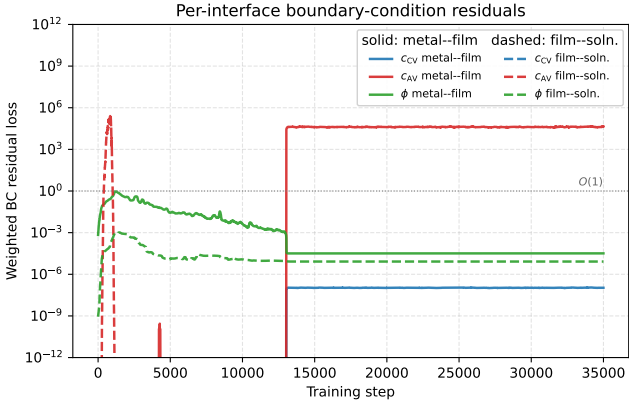


FIG. 11: Per-interface weighted boundary-condition residuals over training. Solid lines are metal/film, dashed lines film/solution, for the cation-vacancy (c_{CV}), anion-vacancy (c_{AV}), and potential (ϕ) constraints. The anion-vacancy residual locks at $\mathcal{O}(10^5)$ after a regime change near step 1.3×10^4 , far above all other components.

weights explores a much larger space and can settle on a

non-physical branch.

Two architectural remedies did not work. Residual connections smoothed the interior loss landscape (Fig. 12), as expected from Li et al.³⁹, but this made things worse by allowing the optimizer to satisfy interior equations more easily while the boundary constraints were neglected. Enforcing positivity of concentrations via a softmax output layer corrupted the gradient information for the film thickness network, yielding correct sign but inaccurate magnitudes.

The hybrid approach circumvents the problem by anchoring the solution to the correct branch with a single data point. The reproducibility of the converged result across independent random-anchor runs (Sec. IV D) confirms that the PINN has already learned the physics correctly; one measurement is enough to eliminate the branch ambiguity.

E. Loss-landscape diagnostics

Loss landscape visualization^{39,40} proved useful for identifying which constraint dominates training difficulties. Following Li et al., we project the parameter space onto

two random filter-normalized directions $\boldsymbol{\eta}$ and $\boldsymbol{\delta}$, and plot

$$f(\alpha, \beta) = \mathcal{L}(\boldsymbol{\theta}^* + \alpha\boldsymbol{\eta} + \beta\boldsymbol{\delta}). \quad (21)$$

Figure 12 shows that the anion vacancy boundary condition dominates the total loss landscape, making it the primary target for future constraint-enforcement improvements.

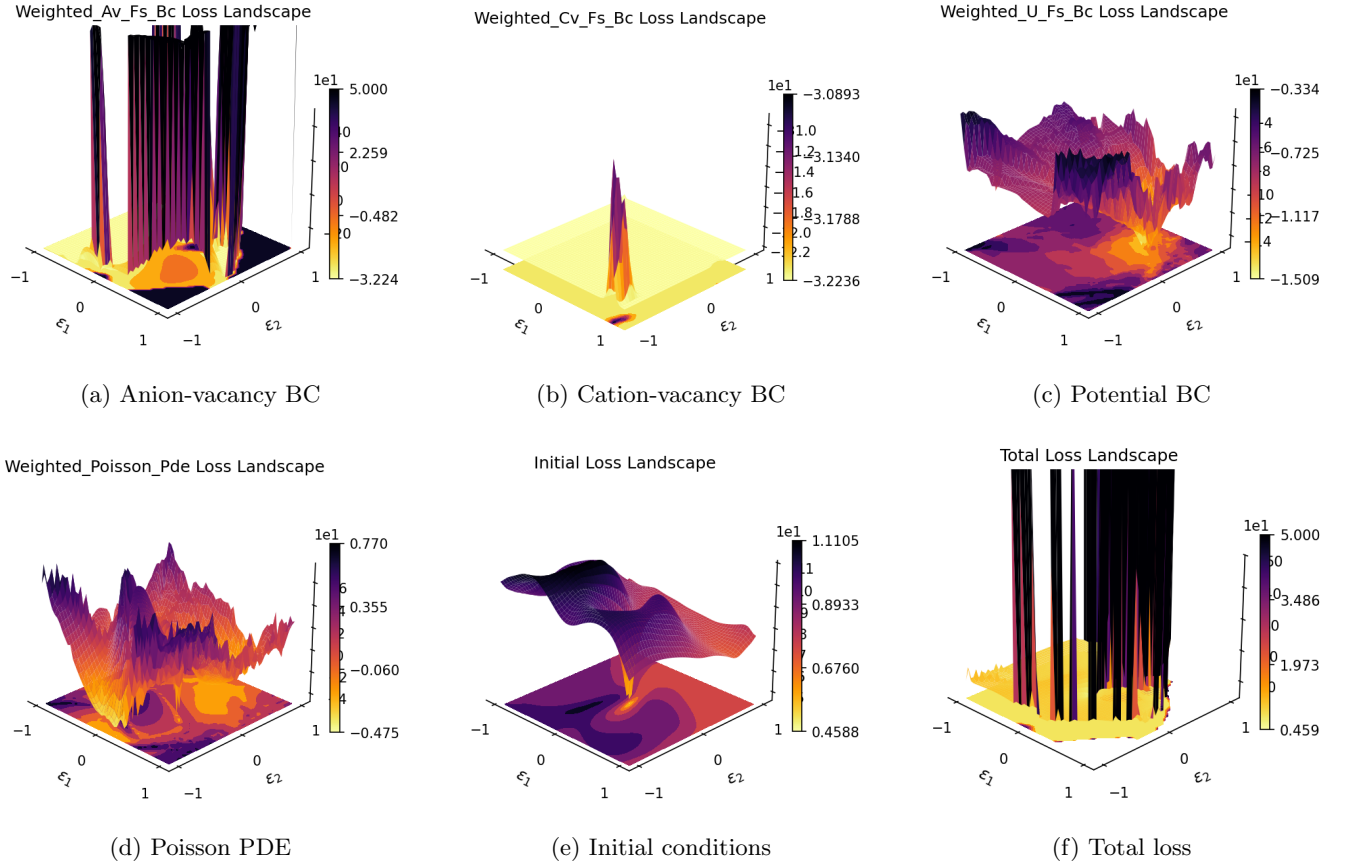


FIG. 12: Loss landscapes around the converged solution, projected onto two filter-normalized directions. The anion-vacancy boundary condition (a) is highly corrugated, whereas the other constraints, such as the cation-vacancy (b) and potential (c) boundary conditions, the Poisson residual (d), and the initial conditions (e), are comparatively smooth. The total landscape (f) is essentially indistinguishable from (a), identifying the anion-vacancy boundary condition as the primary unsatisfied constraint.

VI. DISCUSSION

The central finding is that the four failure modes are separable. The first two, scale disparity and loss imbalance, are fully resolved by existing techniques: physics-based non-dimensionalization and NTK adaptive weighting. Together they bring the pure PINN to qualitatively correct physics. The remaining quantitative error is not a computational pathology but reflects a structural property of the PDE system itself. The coupled Nernst–Planck–Poisson equations under exponential Butler–Volmer boundary conditions define a nonlinear fixed-point problem; the exponential nonlinearity in the boundary terms does not, in general, guarantee a unique solution for arbitrary initial data. Concretely, we observe that different random network initialisations consistently converge to solutions with different absolute thickness scales while achieving comparable interior residuals, the expected signature of a multiple-branch system. Whether this non-uniqueness also manifests in FEM under certain initialisation strategies is an open question that warrants analytical study of the PDM’s solution structure.

The data efficiency of the hybrid approach deserves emphasis. A purely data-driven surrogate for a PDE system of this complexity would require training data spanning the full (x, t, E) space; in practice, generating even a coarse coverage with FEM at 10 potentials and 10 time snapshots produces $\mathcal{O}(10^2)$ labelled solutions, each requiring a separate COMSOL run¹⁰. The hybrid PINN achieves errors below 2.2% with a single FEM-validated point, reducing the FEM workload to a one-time spot check. The natural workflow is to use FEM sparingly as a branch selector rather than a training set, and then rely on the PINN for rapid parameter-space exploration across the full voltage and time range. Training the hybrid model is a one-time cost of about 47 minutes on a single GPU, after which the trained networks return $L(t)$ at any voltage and time in a single inference pass; reproducing the same coverage with FEM requires a separate adaptive-mesh solve for each operating condition¹⁰, and an inverse or design question additionally requires wrapping that solver in an optimisation or adjoint loop. A step-by-step checklist for applying this workflow to new problems, including common warning signs and recommended diagnostic checks, is provided in the SI (Section S4).

The boundary-condition stiffness problem identified in Sec. V C is a known challenge across PINN applications^{24,25}, and our loss-landscape analysis points specifically to the anion vacancy BC as the dominant unsatisfied constraint. This localisation suggests that the path forward is not uniform weight adjustment but structural modification of how that particular constraint is enforced. Structure-preserving PINNs that embed a Lyapunov function consistent with the film-growth thermodynamics⁴¹ could in principle prevent the optimizer from exploring regions of weight space that violate energy monotonicity, directly reducing the size of the problematic loss basin.

Kolmogorov–Arnold networks with adaptive activation functions⁴² offer a complementary route: their per-edge learnable activations can adapt locally near the boundary layer where the anion vacancy gradient is steepest, potentially matching the stiffness scale without requiring an explicit penalty. Energy natural gradient methods^{30,43} address the same problem from the optimisation side, providing second-order curvature information that standard Adam lacks precisely in the flat-loss regions around stiff constraints.

Regarding the PINN’s limitation to fixed geometry: the approach as implemented handles one-dimensional moving boundaries through the film-growth ODE. Extension to two- or three-dimensional geometries would require re-training for each geometry change, as is standard for PINNs²⁴. Finite Basis PINNs⁴⁴ or domain-decomposition approaches could address this limitation and constitute a natural next step.

The methodology developed here (non-dimensionalization, NTK weighting, hybrid anchoring, and loss-landscape diagnostics) is not specific to the PDM. The four failure modes recur whenever a PINN couples stiff transport to nonlinear interface kinetics. In dendritic solidification, for instance, the Nernst–Planck equation for solute is replaced by a heat equation, but the stiffness structure is identical: the solid/liquid interface moves on a time scale set by latent heat release that is orders of magnitude shorter than bulk diffusion, producing the same scale-disparity failure that dimensional PDM training exhibits. Reactive transport in solid electrolytes presents a two-failure-mode problem: Butler–Volmer exchange at grain boundaries provides the non-unique branch structure, while the wide range of ionic conductivities across phases produces the loss imbalance. In both cases the hybrid anchoring strategy, which uses a single validated reference solution to select the physical branch, transfers without modification.

VII. CONCLUSIONS

We have shown that physics-informed neural networks can solve the Point Defect Model of passive-film growth and, more valuably, recover its kinetic parameters from sparse data, a problem central to predicting material degradation and one for which conventional approaches lean on specialised FEM solvers and costly experiments. The PDM is difficult for reasons common to stiff multi-physics systems rather than peculiar to it: widely separated scales, stiff boundary conditions, and convergence to non-physical solution branches. We handled the first with physics-based non-dimensionalisation (stable simulation from about one hour to 250 hours), the second with NTK adaptive weighting (a four-to-six-order loss imbalance compressed to roughly one), and the branch ambiguity with a single validated anchor that brings film-thickness error below 2.2% at all five potentials; stiff boundary-condition enforcement resisted every weighting

scheme and remains open, with a boundary-residual and loss-landscape analysis localising it to the anion-vacancy condition. The result is robust because the anchor is resampled at every step, accuracy saturates beyond about ten anchors, and the physics loss tolerates roughly 5% measurement noise. The practical payoff is that this anchor can be a single experiment: from sparse measurements the framework reconstructs the full coupled solution and infers unknown kinetic constants, with recoverability tracking stiffness (the boundary-stiff rate constant is identifiable, the weakly-coupled interior coefficient is not). By turning a few measurements into full fields and calibrated kinetics, it reduces the experimental and computational burden of studying passive-film growth, and the same recipe transfers to other stiff transport–reaction systems with moving boundaries.

SUPPLEMENTARY MATERIAL

See the supplementary material for the complete interfacial reaction schemes, the characteristic scales and full non-dimensionalisation of the governing equations, a table of all model parameters with values and units, practical guidelines for applying the framework to new stiff multiphysics problems, additional training-loss curves, the random-anchor robustness analysis, and the inverse-problem setup.

ACKNOWLEDGMENTS

This work was supported by the NSERC–CNSC Small Modular Reactors Research Grant Initiative (ALLRP 580475-2022). This work was made possible by the facilities of the Shared Hierarchical Academic Research Computing Network (SHARCNET:www.sharcnet.ca) and Digital Research Alliance of Canada (<https://alliancecan.ca/en>).

AUTHOR CONTRIBUTIONS

Mohid Farooqi: Conceptualization (equal); Software (lead); Formal analysis (lead); Investigation (lead); Visualization (lead); Writing – original draft (lead); Writing – review & editing (equal). **Ingmar Bösing**: Resources (lead); Data curation (lead); Writing – review & editing (supporting). **Conrard Giresse Tetsassi Feugmo**: Conceptualization (lead); Supervision (lead); Funding acquisition (lead); Software (supporting); Writing – original draft (supporting); Writing – review & editing (equal).

DATA AVAILABILITY STATEMENT

The Python implementation of the PINNACLE training framework, all model parameters, and scripts to re-

produce all figures in this paper are available at <https://github.com/Feugmo-Group/PINNACLE> under an open-source MIT licence. FEM reference data are included in the repository in tabular form. Scripts to reproduce the ablation, robustness, data-efficiency, noise, and inverse-problem experiments reported in Sec. IV are provided in the `scripts/` directory, and the Hydra configuration used for all reported runs is provided under `conf/`.

- ¹T. Singh and E. Kohn, “Harsh Environment Materials,” in *Reference Module in Materials Science and Materials Engineering* (Elsevier, 2016).
- ²H. J. Fu, P. Buabthong, Z. P. Ifkovits, W. Yu, B. S. Brunschwig, and N. S. Lewis, “Catalytic open-circuit passivation by thin metal oxide films of p-si anodes in aqueous alkaline electrolytes,” *Energy & Environmental Science* **15**, 334–345 (2021).
- ³L. Ma, F. Wiame, V. Maurice, and P. Marcus, “Origin of nanoscale heterogeneity in the surface oxide film protecting stainless steel against corrosion,” *npj Materials Degradation* **3**, 29 (2019).
- ⁴V. Maurice and P. Marcus, “Current developments of nanoscale insight into corrosion protection by passive oxide films,” *Current Opinion in Solid State and Materials Science* **22**, 156–167 (2018), 1807.10689.
- ⁵D. D. Macdonald, “The history of the Point Defect Model for the passive state: A brief review of film growth aspects,” *Electrochimica Acta* **56**, 1761–1772 (2011).
- ⁶M. Iannuzzi and G. S. Frankel, “The carbon footprint of steel corrosion,” *npj Materials Degradation* **6**, 101 (2022).
- ⁷A. Al-Amieri, W. N. R. Wan Isahak, and W. K. Al-Azzawi, “Sustainable corrosion inhibitors: A key step towards environmentally responsible corrosion control,” *Ain Shams Engineering Journal* **15**, 102672 (2024).
- ⁸A. Seyeux, V. Maurice, and P. Marcus, “Oxide Film Growth Kinetics on Metals and Alloys: I. Physical Model,” *Journal of The Electrochemical Society* **160**, C189–C196 (2013).
- ⁹K. Leistner, C. Toulemonde, B. Diawara, A. Seyeux, and P. Marcus, “Oxide Film Growth Kinetics on Metals and Alloys: II. Numerical Simulation of Transient Behavior,” *Journal of The Electrochemical Society* **160**, C197–C205 (2013).
- ¹⁰I. Bösing, “Modeling electrochemical oxide film growth—passive and transpassive behavior of iron electrodes in halide-free solution,” *npj Materials Degradation* **7**, 53 (2023).
- ¹¹N. Alexiadis, A. Fuchs, T. Troßmann, I. Bösing, J. Thöming, and F. L. Mantia, “Modeling and simulation of passive film formation and breakdown in chloride ion containing electrolytes – a point defect model extension,” *Corrosion Science* **256**, 113166 (2025).
- ¹²Y. Li, D. D. Macdonald, J. Yang, J. Qiu, and S. Wang, “Point defect model for the corrosion of steels in supercritical water: Part I, film growth kinetics,” *Corrosion Science* **163**, 108280 (2020).
- ¹³D. Kolotinskii, V. Nikolaev, V. Stegailov, and A. Timofeev, “Point Defect Model for the kinetics of oxide film growth on the surface of T91 steel in contact with lead–bismuth eutectic,” *Corrosion Science* **211**, 110829 (2023).
- ¹⁴G. R. Engelhardt, D. Chen, C. Dong, and D. D. Macdonald, “Estimation of some parameters in the point defect model (PDM) for the passivity of metals,” *Journal of The Electrochemical Society* **171**, 031503 (2024).
- ¹⁵C. Bataillon, F. Bouchon, C. Chainais-Hillairet, J. Fuhrmann, E. Hoarau, and R. Touzani, “Numerical methods for the simulation of a corrosion model with moving oxide layer,” *Journal of Computational Physics* **231**, 6213–6231 (2012).
- ¹⁶L. Sun, T. Zhao, J. Qiu, Y. Sun, K. Li, H. Zheng, Y. Jiang, Y. Li, J. Li, W. Li, and D. D. Macdonald, “Point defect model for passivity breakdown on hyper-duplex stainless steel 2707 in solutions containing bromide at different temperatures,” *Corrosion Science* **194**, 109959 (2022).
- ¹⁷M. Raissi, P. Perdikaris, and G. E. Karniadakis, “Physics-informed neural networks: A deep learning framework for solving forward

- and inverse problems involving nonlinear partial differential equations,” *Journal of Computational Physics* **378**, 686–707 (2019).
- ¹⁸H. Chen, E. Kästelhön, and R. G. Compton, “Predicting voltammetry using physics-informed neural networks,” *The Journal of Physical Chemistry Letters* **13**, 536–543 (2022).
- ¹⁹H. Chen, C. Batchelor-McAuley, E. Kästelhön, J. Elliott, and R. G. Compton, “A critical evaluation of using physics-informed neural networks for simulating voltammetry: Strengths, weaknesses and best practices,” *Journal of Electroanalytical Chemistry* **925**, 116918 (2022).
- ²⁰H. Chen, E. Kästelhön, and R. G. Compton, “The application of physics-informed neural networks to hydrodynamic voltammetry,” *Analyst* **147**, 1881–1891 (2022).
- ²¹S. Kathane and S. Karagadde, “A Physics Informed Neural Network (PINN) Methodology for Coupled Moving Boundary PDEs,” (2024), arXiv:2409.10910 [cs].
- ²²N. Chen, S. Lucarini, R. Ma, A. Chen, and C. Cui, “PF-PINNs: Physics-informed neural networks for solving coupled allen-cahn and cahn-hilliard phase field equations,” *Journal of Computational Physics* **529**, 113843 (2025).
- ²³W. Li, R. Fang, J. Jiao, G. N. Vassilakis, and J. Zhu, “Tutorials: Physics-informed machine learning methods of computing 1D phase-field models,” *APL Machine Learning* **2**, 031101 (2024).
- ²⁴J. D. Toscano, V. Oommen, A. J. Varghese, Z. Zou, N. A. Daryak-enari, C. Wu, and G. E. Karniadakis, “From PINNs to PIKANs: Recent Advances in Physics-Informed Machine Learning,” (2024), arXiv:2410.13228 [cs].
- ²⁵A. A. Sophiya, A. K. Nair, S. Maleki, and S. K. Krishnababu, “A comprehensive analysis of PINNs: Variants, Applications, and Challenges,” (2025), arXiv:2505.22761 [cs].
- ²⁶R. Sun, H. Jeong, J. Zhao, Y. Gou, E. Sauret, Z. Li, and Y. Gu, “A physics-informed neural network framework for multi-physics coupling microfluidic problems,” *Computers & Fluids* **284**, 106421 (2024).
- ²⁷A. Al-Safwan, C. Song, and U. b. Waheed, “Is it time to swish? Comparing activation functions in solving the Helmholtz equation using physics-informed neural networks,” (2021), arXiv:2110.07721 [physics].
- ²⁸A. Jacot, F. Gabriel, and C. Hongler, “Neural Tangent Kernel: Convergence and Generalization in Neural Networks,” (2020), arXiv:1806.07572 [cs].
- ²⁹S. Wang, X. Yu, and P. Perdikaris, “When and why PINNs fail to train: A neural tangent kernel perspective,” *Journal of Computational Physics* **449**, 110768 (2022).
- ³⁰J. Müller and M. Zeinhofer, “Achieving High Accuracy with PINNs via Energy Natural Gradients,” (2023), arXiv:2302.13163 [cs].
- ³¹M. Raissi, A. Yazdani, and G. E. Karniadakis, “Hidden fluid mechanics: Learning velocity and pressure fields from flow visualizations,” *Science* **367**, 1026–1030 (2020).
- ³²Z. Chen, Y. Liu, and H. Sun, “Physics-informed learning of governing equations from scarce data,” *Nature Communications* **12**, 6136 (2021).
- ³³V. Trávníková, E. Von Lieres, and M. Behr, “Quantifying data needs in surrogate modeling for flow fields in two-dimensional stirred tanks with physics-informed neural networks,” *Physics of Fluids* (2025).
- ³⁴S. Bhatnagar, A. Comerford, and A. Banaeizadeh, “Physics-informed neural networks for modeling of 3D flow–thermal problems with sparse domain data,” *Journal of Machine Learning for Modeling and Computing* **5**, 39–67 (2024).
- ³⁵S. Cuomo, V. S. Di Cola, F. Giampaolo, G. Rozza, M. Raissi, and F. Piccialli, “Scientific machine learning through physics-informed neural networks: Where we are and what’s next,” *Journal of Scientific Computing* **92**, 88 (2022).
- ³⁶N. Malekjani, A. Kharaghani, and E. Tsotsas, “A comparative study of dimensional and non-dimensional inputs in physics-informed and data-driven neural networks for single-droplet evaporation,” *Chemical Engineering Science* **306**, 121214 (2025).
- ³⁷H. Son, S. W. Cho, and H. J. Hwang, “Enhanced Physics-Informed Neural Networks with Augmented Lagrangian Relaxation Method (AL-PINNs),” (2023), arXiv:2205.01059 [cs].
- ³⁸Y. W. Bekele, “PHYSICS-INFORMED NEURAL NETWORKS WITH CURRICULUM TRAINING FOR POROELASTIC FLOW AND DEFORMATION PROCESSES,” *Computers and Geotechnics* (2024).
- ³⁹H. Li, Z. Xu, G. Taylor, C. Studer, and T. Goldstein, “Visualizing the Loss Landscape of Neural Nets,” (2018), arXiv:1712.09913 [cs].
- ⁴⁰S. Basir, “Investigating and Mitigating Failure Modes in Physics-informed Neural Networks (PINNs),” *Communications in Computational Physics* **33**, 1240–1269 (2023), arXiv:2209.09988 [cs].
- ⁴¹H. Chu, Y. Miyatake, W. Cui, S. Wei, and D. Furihata, “Structure-preserving physics-informed neural networks with energy or lyapunov structure,” in *Proceedings of the Thirty-Third International Joint Conference on Artificial Intelligence* (2024) pp. 3872–3880.
- ⁴²Z. Zhang, Q. Wang, Y. Zhang, T. Shen, and W. Zhang, “Physics-informed neural networks with hybrid Kolmogorov-Arnold network and augmented Lagrangian function for solving partial differential equations,” *Scientific Reports* **15**, 10523 (2025), publisher: Nature Publishing Group.
- ⁴³A. Guzmán-Cordero, F. Dangel, G. Goldshlager, and M. Zeinhofer, “Improving Energy Natural Gradient Descent through Woodbury, Momentum, and Randomization,” (2025), arXiv:2505.12149 [cs].
- ⁴⁴B. Moseley, A. Markham, and T. Nissen-Meyer, “Finite Basis Physics-Informed Neural Networks (FBPINNs): a scalable domain decomposition approach for solving differential equations,” *Advances in Computational Mathematics* **49** (2023), 10.1007/s10444-023-10065-9, arXiv:2107.07871 [physics].